LAWRENCE
LIVERMORE
NATIONAL
LABORATORY

Measuring the angular dependence of betatron x-ray spectra in a laser-wakefield accelerator

F. Albert, B. Pollock, J. L. Shaw, K. A. Marsh, J. E. Ralph, Y. H. Chen, D. Alessi, A. Pak, C. E. Clayton, S. H. Glenzer, C. Joshi

January 21, 2015

Measuring the angular dependence of betatron x-ray spectra in a laser-wakefield accelerator

F. Albert[1*], B. B. Pollock[1], J. L. Shaw[2], K. A. Marsh[2], J. E. Ralph[1], Y.-H. Chen[1], D. Alessi[1], A. Pak[1], C. E. Clayton[2], S. H. Glenzer[3] and C. Joshi[2]

[1]Lawrence Livermore National Laboratory, NIF and Photon Sciences, 7000 East Avenue, Livermore CA 94550, USA

[2]Department of Electrical Engineering, University of California, Los Angeles CA 90095, USA

[3]SLAC National Accelerator Laboratory, Stanford CA 94309, USA

E-mail: `albert6@llnl.gov`

Abstract. This paper presents a new technique to measure the angular dependence of betatron x-ray spectra in a laser-wakefield accelerator. Measurements are performed with a stacked image plates spectrometer, capable of detecting broadband x-ray radiation up to 1 MeV. It can provide measurements of the betatron x-ray spectrum at any angle of observation (within a 40 mrad cone) and of the beam profile. A detailed description of our data analysis is given, along with comparison for several shots. These measurements provide useful information on the dynamics of the electrons are they are accelerated and wiggled by the wakefield.

1. Introduction

One of the most notable applications of laser-wakefield accelerators (LWFAs) [1, 2, 3, 4] is the production of light sources with novel properties. For example, betatron x-ray radiation is produced when electrons are accelerated at an ultrahigh gradient in a LWFA. In the three-dimensional (3D), highly nonlinear LWFA regime, when a short laser pulse with an intensity $I > 10^{18}$ W/cm^2 is focused inside a plasma, the laser ponderomotive force completely expels the plasma electrons away from the strong intensity regions to form an ion bubble in the wake of the pulse. Electrons trapped at the back of this structure are accelerated and wiggled by the focusing force of the more massive and immobile ions to produce broadband, synchrotron-like radiation in the keV energy range.

The theoretical properties of betatron x-ray radiation are well known [5]; it was first observed in a beam-driven plasma channel [6] and later in a laser-driven one [7, 8, 9]. Since these first observations were made, betatron x-ray generation has been an extremely prolific field of research within the LWFA community. High-quality studies have been carried out at a number of high-intensity laser facilities worldwide and have implied that betatron x-rays have a source size of a few microns [10, 9], a divergence of less than 100 mrad [11], a pulse duration of less than 100 fs [12], and a broadband spectrum in the keV energy range [13, 14]. Betatron x-rays are also directly related to the electrons emitting them, and thus the radiative properties of the source can be an excellent diagnostic of the LWFA acceleration process. The electron beam emittance and size have been inferred in experiments from the x-ray beam profile [11, 15], spectrum [16, 17], or source size [18]. However, the imaging or spectroscopy techniques traditionally used to characterize betatron x-ray radiation do not provide detailed simultaneous information on the x-ray source spectrum and beam profile.

In this paper, we present a new diagnostic, and subsequent data analysis, to measure the angular dependence of betatron x-ray spectra in a LWFA. This diagnostic consists of a stacked image plates spectrometer with differential filtering, and it has enabled us to observe betatron x-rays with energies extending up to 80 keV during experiments performed at the Lawrence Livermore National Laboratory's Jupiter Laser Facility. The paper is organized as follows: Section 2 presents the radiation models used for our data analysis, Section 3 gives a description of the experimental setup, Section 4 gives a detailed description, along with calibration data, of our stacked image plates spectrometer, Section 5 shows the details of our analysis for a single shot and a comparison between several shots, and finally Section 6 discusses possible hypotheses to explain the observed spectral and spatial properties of the source in our experiments.

2. Betatron radiation modeling tools

There are several methods to model betatron x-ray radiation in a LWFA. Electron trajectories obtained from Particle In Cell (PIC) codes, such as OSIRIS, can be post-

processed to calculate the radiation beam profile and spectrum with excellent accuracy [19]. This is, however, computationally intensive, and betatron radiation can also be easily modeled with single electron trajectories.

In our model, the motion of an electron accelerated along $\vec{u_z}$ with momentum $\vec{p}$ and position $\vec{r}$ in the wake of a laser pulse is described by the Lorentz equation of motion:

$$\frac{d\vec{p}}{dt} = -m\omega_p^2 \frac{\vec{r}}{2} + \alpha \frac{mc\omega_p}{e} \vec{u_z},$$ (1)

where m is the electron rest mass, e the elementary charge, and $\omega_p = \sqrt{n_e e^2/m\epsilon_0}$ is the plasma frequency. Here, n_e is the electron density, and ϵ_0 the vacuum permittivity. In the blowout 3D nonlinear regime of laser wakefield acceleration [20], $\alpha = \frac{1}{2}\sqrt{a_0}$ is the normalized accelerating field, where a_0 is the laser normalized vector potential. Equation 1 is solved by using a 4th order Runge-Kutta algorithm to obtain the single electron trajectories for given initial conditions and fields. The electron position and momentum are used to calculate the intensity radiated by the particle per unit frequency ω and solid angle Ω [21]:

$$\frac{d^2 I}{d\Omega d\omega} = \frac{e^2 \omega^2}{4\pi c} \left| \int_{-\infty}^{\infty} \vec{n} \times (\vec{n} \times \beta) e^{i\omega(t - \frac{\vec{n}.\vec{r}}{c})} dt \right|^2,$$ (2)

where $\vec{n}$ is the vector corresponding to the direction of observation, and $\beta = v/c$ is the normalized electron velocity. In the case where the wiggler parameter $K = 1.33 \times 10^{-10}\sqrt{\gamma n_e} r_0$ is larger than unity, the spectrum, observed at an angle θ from the plane in which the particle oscillates, can be approximated by the asymptotic limit [5, 21]:

$$\frac{d^2 I}{d\Omega d\omega} = \frac{e^2}{3\pi^2 c} \left(\frac{\omega\rho}{c}\right)^2 \left(\frac{1}{\gamma^2} + \theta^2\right) \left[K_{2/3}^2(\xi) + \frac{\theta^2}{(1/\gamma^2) + \theta^2} K_{1/3}^2(\xi)\right],$$ (3)

where $K_{2/3}$ and $K_{1/3}$ are modified Bessel functions. Here, ρ is the radius of curvature of the electron trajectory and $\xi = \frac{\omega\rho}{3c}\left(\frac{1}{\gamma^2} + \theta^2\right)^{3/2}$.

The betatron x-ray beam profile is calculated by integrating Eq. 2 over frequencies, and the betatron x-ray spectrum integrated over angles is:

$$\frac{dI}{d\omega} = \sqrt{3}\frac{e^2}{c}\gamma\frac{\omega}{\omega_c} \int_{\frac{\omega}{\omega_c}}^{\infty} K_{5/3}(x)dx,$$ (4)

where $K_{5/3}$ is also a modified Bessel function and $\omega_c = 3\gamma^3 c/\rho$ is the critical frequency. For $\theta = 0$, Eq. 3 is maximum for a peak energy of $\omega \sim 0.45\omega_c$. For larger θ, the peak frequency is lower.

Fig. 1 shows an example of a calculated electron trajectory, with its corresponding betatron x-ray spectrum and beam profile. For this particular case, the parameters are $n_e = 10^{19}$ cm^{-3}, $\gamma = 200$, $x_0 = 1$ μm, $y_0 = 0$, and $\alpha = 0$ (constant energy). The trajectory is calculated using 3000 time steps (with each unit step $dt = 0.2/\omega_p$). At each point of calculation of the trajectory, the spectrum and beam profile are calculated using frequency steps of 100 eV. For the chosen parameters, $\omega_c = 4.2$ keV and $K \simeq 6$. The beam has a divergence of $1/\gamma$ and K/γ along the direction parallel and perpendicular to the plane of the electron oscillations, and the on-axis spectrum peaks at ~ 2 keV.
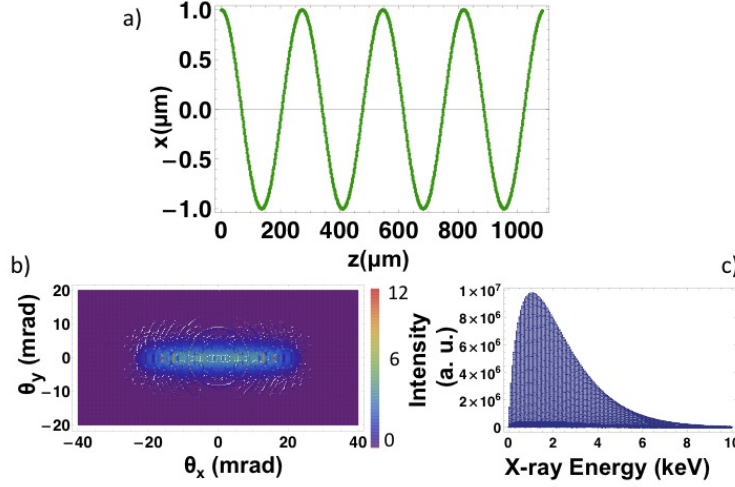
Figure 1. Example of an electron trajectory in the plasma (a), with the corresponding betatron x-ray beam profile (b) and spectrum observed on axis (c), calculated using Eq. 2 and containing the harmonic structure of the radiation. For this example, the parameters are $n_e = 10^{19}$ cm^{-3}, $\gamma = 200$, $x_0 = 1$ μm, $y_0 = 0$, and $\alpha = 0$. Here the critical frequency $\hbar\omega_c = 4.2$ keV and $K \simeq 6$. The beam has a divergence of $1/\gamma$ and K/γ along the direction parallel and perpendicular to the plane of the oscillations..

3. Experiment

We performed experiments at the Jupiter Laser Facility (JLF), Lawrence Livermore National Laboratory, using the Callisto laser system. Callisto is a 200 TW laser and delivers pulses of 60 fs (full width at half maximum, fwhm) duration with energies up to 12 J at a repetition rate of 1 shot/30 min. The experimental setup is shown in Fig. 2. Using an f/8 off-axis parabola, we focus the laser onto the edge of a 6 mm or 10 mm gas cell, with respectively 500 μm and 1 mm entrance and exit pinholes. The focal spot, measured at low laser power, is 12 μm (fwhm), and $a_0 \sim 2$. The background electron density of the plasma is measured with interferometry by using a 100 fs probe pulse synchronized with the main laser pulse. The density is deduced from the fringe shift on the raw data by using an Abel inversion code. As shown in Fig. 2, the electrons are vertically deflected by a 0.42 Tesla, 21.5-cm-long permanent dipole magnet onto two image plates (model FUJI-MS-2040), IP$_a$ and IP$_b$ (a two-screen electron spectrometer [22, 23, 24]). Two image plates are needed to calculate both the electron energy and deflection from the laser propagation axis when they exit the plasma [25]. The betatron x-rays propagate outside of the vacuum target chamber through a 65 μm mylar window and a 50 μm Al filter to block any residual laser light. The betatron beam profile is measured on IP$_a$, and after transmission through IP$_a$, the stacked image plates spectrometer measures the beam profile and spectrum.
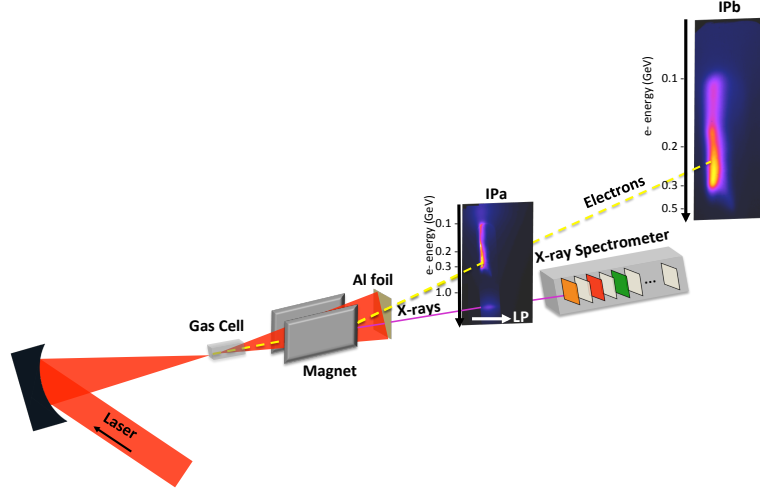
Figure 2. Schematic of the experimental setup at JLF, showing the 800 nm, 60 fs laser focused onto the gas cell with the f/8 off-axis parabola. The electrons (dashed line) are deflected by the 21 cm long, 0.42 Tesla magnet centered on the laser axis and located 3.5 cm from the source, inside the target chamber. The particles successively hit the first and second image plate (IP_a and IP_b, located 37.2 cm and 111.1 cm away from the magnet exit, respectively). The laser is blocked by a 50 μm Al foil (combined with a 65 μm mylar window at the vacuum/air interface of the target chamber) to block residual laser light. The x-rays (solid line) propagate through 7.3 cm of air and through IP_a onto the 15 channel x-ray spectrometer.

4. Stacked image plates spectrometer for betatron radiation

4.1. Design

A schematic of the stacked image plates spectrometer is shown in Fig. 2. It consists of 15 1 inch × 1 inch image plates (model FUJI-MS) stacked in a light-tight lexan cartridge with a square aperture in front. Filters, arranged by increasing Z number (and thickness for channels 10-15), are placed in front of each image plate. For our experiments, the aluminum filter is placed against the aperture, followed by the first image plate. The design of this diagnostic has been adapted from Chen et al [26], where it was originally used to measure bremsstrahlung radiation from hot electrons in fast ignition experiments. Since the betatron spectrum is not isotropic, we are not using a collimator and the front aperture is larger to be able to detect the beam. This diagnostic can in principle detect and spectrally resolve broadband x-ray radiation up to 1 MeV through the 15 successive channels, with an acceptance angle of 40 mrad in our experimental configuration. However, x-ray spectra from betatron radiation produced in our experiments only extend up to $\sim$ 80 keV. As a result, we are only seeing signal up to the 5th channel of the spectrometer. This diagnostic works well for detecting betatron radiation above 5 keV, but is not suited for lower energy x-rays, due to the reduced sensitivity of image plates below this energy and to the fact that the MS image plates have a ferromagnetic layer stacked behind the sensitive layer [27].

4.2. Spectrometer response to a betatron x-ray spectrum

The response of each of the 15 channels of the spectrometer (behind the corresponding filter) is shown in Fig. 3, up to photon energies of 1 MeV. It was obtained with a one dimensional model, calculated with the Monte Carlo simulation package Integrated Tiger Series 3.0. It tracks electron and x-ray/gamma-ray photons through the spectrometer, taking into account effects such as scattering, pair production, and x-ray fluorescence. This model has been calibrated up to 662 keV, and comparison with other instruments, such as transmission crystal spectrometers, have shown reasonable agreement. The calibration was made with ^{109}Cd (22 keV) and ^{137}Cs (662 keV) radioactive sources. When image plates are exposed to x-ray radiation, electrons in the phosphor (sensitive) laser are excited and kept in a metastable state. These are liberated when they are scanned with red laser light, resulting in the emission of blue photons detected by a photomultiplier tube. After each shot, the image plates were kept in the lexan cartridge and light-tight box, and scanned 10 minutes after x-ray exposure with a FLA-7000 scanner, which reads photostimulated luminescence (PSL) values. Fig. 4 shows the expected dose produced on the spectrometer channels for betatron spectra with critical energies $\hbar\omega_c$ = 5, 10, 15, 20 and 30 keV. The spectra are calculated by using the function $(\omega/\omega_c)^2 K_{2/3}^2(\omega/\omega_c)$ (Eq. 3 for $\theta = 0$ and fixed arbitrary γ), where $\hbar\omega_c$ is varied accordingly. Each intensity spectrum is then converted into units of photon/eV and propagated through the different elements of the experiment (Al, mylar window, air and IP$_a$), where transmission curves are shown in the inset of Fig 4 (a) for our experimental configuration. The expected integrated dose produced on each spectrometer channel is finally calculated by convoluting each spectrum with the response functions shown in Fig. 3. The spectrometer can thus detect betatron radiation with a wide range of critical energies.

5. Results and analysis

A detailed analysis of betatron x-ray data on the stacked image plates spectrometer has recently shown that, in our experimental conditions, the angular dependence of betatron x-ray spectra suggests an anisotropic distribution of the electron energy spectrum [28]. In this section, we show additional data, a detailed description of the analysis procedure and subsequent interpretation of the results. We first describe the analysis for a given shot, and provide some comparisons with shots done under similar experimental conditions.

5.1. Single-shot analysis

5.1.1. Electron spectrum Fig. 5 shows, for a given shot, the electron data recorded on IP$_a$ and IP$_b$ and the corresponding electron beam spectrum. It has a maximum electron energy of 268 ± 25 MeV. The error bar represents the uncertainty on the maximum measured energy, due to the limited resolution of our magnetic spectrometer. For this
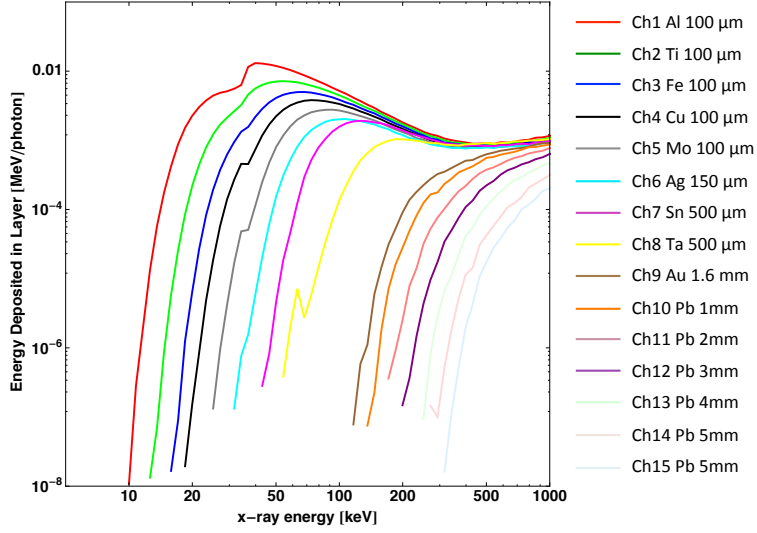
Figure 3. Calculated response of the 15 spectrometer channels, behind their corresponding filter. It represents the energy deposited in each channel by the x-ray photon spectrum.
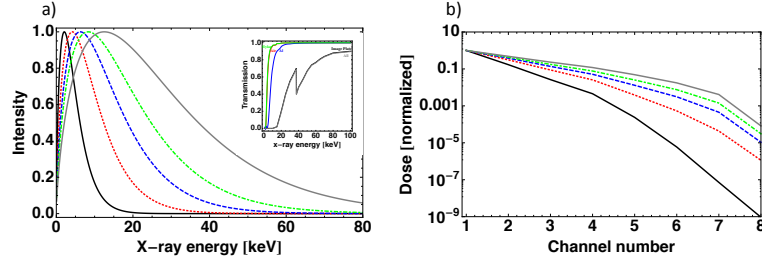

Figure 4. (a) Betatron x-ray spectra with critical energies of 5, 10, 15, 20 and 30 keV (solid, dotted, dashed, dot-dahed and gray lines, respectively). The inset shows the transmission curves for all the elements on the x-ray beam path before the spectrometer. (b) Calculated integrated dose, for channel 1-8, for each spectrum shown in (a).

particular shot, the experimental parameters are laser energy $E = 5.3$ J, $a_0 = 2.33$, and a gas cell filled with 100 % He at $n_e = 6 \times 10^{18}$ cm^{-3}. Due to the highly nonlinear nature of the blowout regime and its sensitivity to nonideal laser beam and plasma density profiles, the electron beam spectrum is not monoenergetic as expected from the theory [20].

5.1.2. On-axis x-ray spectral analysis The first step in our analysis is to retrieve the electron oscillation amplitude in the plasma. This is done using the x-ray spectral data. Fig. 6 shows the average on-axis x-ray dose, deposited in each x-ray spectrometer channel, within a spot centered on the beam profile and subtending a solid angle of $\sim 1.1 \times 10^{-6}$ sr from the source. We have fitted the data (dots) with three different
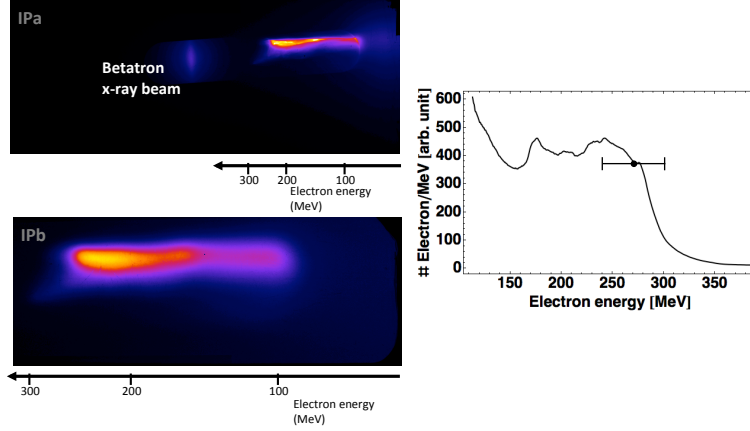
Figure 5. (Left) Electron spectra recorded on the two-screen image plate spectrometer (IP$_a$ and IP$_b$), and (right) corresponding calculated energy spectrum.

theoretical spectra, shown in the inset of Fig. 6. This calculated signal takes into account the filters of our setup (Al, mylar, air, first image plate) and the response function of each detector channel. In the plasma, the electron oscillation radius damps as it is accelerated up to its final energy, and the spectrum critical energy is not constant throughout the trajectory. A detailed analysis (red solid curve) takes this into account and the spectrum (inset) is calculated numerically as follows.

First, the trajectory is calculated by solving Eq. 1 with a 4th order Runge-Kutta algorithm. All parameters and initial conditions needed to solve Eq. 1, except for the initial oscillation radius r_0, are determined by the experimental conditions. The electron density is $n_e = 6 \times 10^{18}$ cm^{-3}, $\alpha = 0.763$, the electron final energy is 268 MeV ($\gamma \simeq 520$), and the electron initial energy is $\gamma_\Phi = \omega_0/\sqrt{3}\omega_p = 9.85$ [20], which is the Lorentz factor corresponding to the phase velocity of the plasma wave. In our simulation, we use 1500 time steps (with each step $dt = 0.4/\omega_p$) for the whole trajectory. At each time step, the corresponding on axis ($\theta = 0$) spectrum is calculated with Eq. 2 and accumulated over the whole trajectory. We adjust the initial radius to $r_0 = 5$ μm so that it fits the upper part of the error bars in our data. An upper bound $r_0 = 5$ μm is consistent with previous measurements [11, 10, 18].

The other spectra shown in the inset are calculated using the function $(\omega/\omega_c)^2 K_{2/3}^2(\omega/\omega_c)$ (Eq. 3 for $\theta = 0$ and fixed arbitrary γ) with parameters $\hbar\omega_c = 15$ keV and $\hbar\omega_c = 20$ keV. This is equivalent to a spectrum produced by a single electron oscillating with a constant amplitude and energy (no acceleration). This simple model estimates the on-axis spectrum critical energy $\hbar\omega_c \sim 15 - 20$ keV (peak energy of 7.5-10 keV).

5.1.3. Beam profile analysis and orientation of electron trajectories The second step is to retrieve the spatial orientation of the electron trajectories. For this, Eq. 2 is used to self consistently match the observed and calculated beam profiles. The experimental
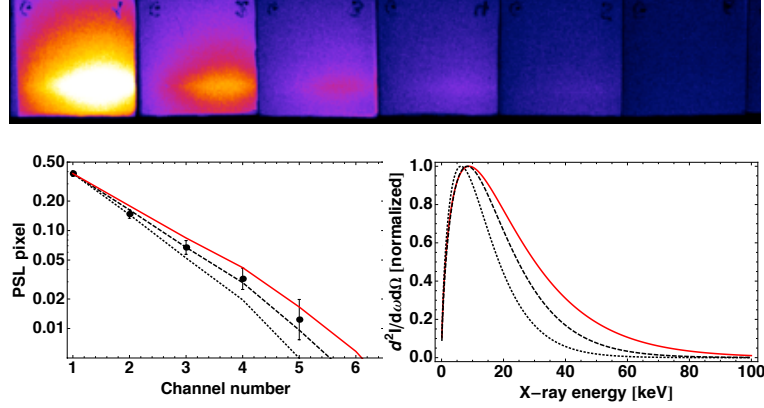
Figure 6. (Top) X-ray data, recorded on the stacked image plates spectrometer for channel 1-6. (Left) X-ray spectrometer dose (dots with error bars), in photostimulated luminescence, PSL, per pixel. Calculated dose (normalized to the first data point), for betatron spectra with critical energies of 15 keV and 20 keV (dotted and dashed lines, respectively) and radiation produced by an electron injected 5 μm off-axis and accelerated up to 268 MeV (red solid line). (Right) Inferred normalized energy distribution spectrum for each case.

(recorded on IP$_a$) and simulated beam profiles are shown in Fig. 7 (a). Their shape is not completely elliptical as one would expect from a single electron oscillating about the axis [11]. To reproduce the experimental profile using a single particle trajectory tracking method, we use Eq. 2 to map the full spatial and spectral distribution of the betatron radiation. Using a least-squares fitting method, the orientation of electron trajectories for four groups of electrons is adjusted until the simulated beam profile matches the experiment. For the simulation, the particles are distributed on a circle of radius $r_0 = 5$ μm in the transverse (x, y) plane with angular steps of $\pi/30$, as shown in Fig 7 (c). Here $\theta = 0$ is along the x axis, the laser is polarized along y ($\theta = \pi/2$). In Fig 7 (b), we show this number of electrons as a function of θ, and for four groups of electrons with different final energies representative of the overall measured spectrum displayed in Fig. 5 (with extrapolation for the lower electron energies). This range of energies is due to the fact that the electron spectrum is not monoenergetic and that electrons were injected into the wake at different times. For each trajectory, the dephasing length is L_{dp}=0.29 cm, and electrons injected later into the wake end with a lower final energy. This reconstruction is specific to our model, in which we assume (i) complete blowout, (ii) electrons trapped in only the first bucket of the wake, and (iii) cylindrical symmetry in the radial focusing forces.

5.1.4. Angular dependence of the betatron x-ray spectrum The third step is to compare the experimental angular dependence of the betatron x-ray spectrum with the angular dependence of the spectrum calculated from the trajectories of Fig. 7. Fig. 8 shows the variation of the peak x-ray energy with the observation angle, the latter is defined in the inset. For each observation angle, we measure the dose in channels 1-6 of the
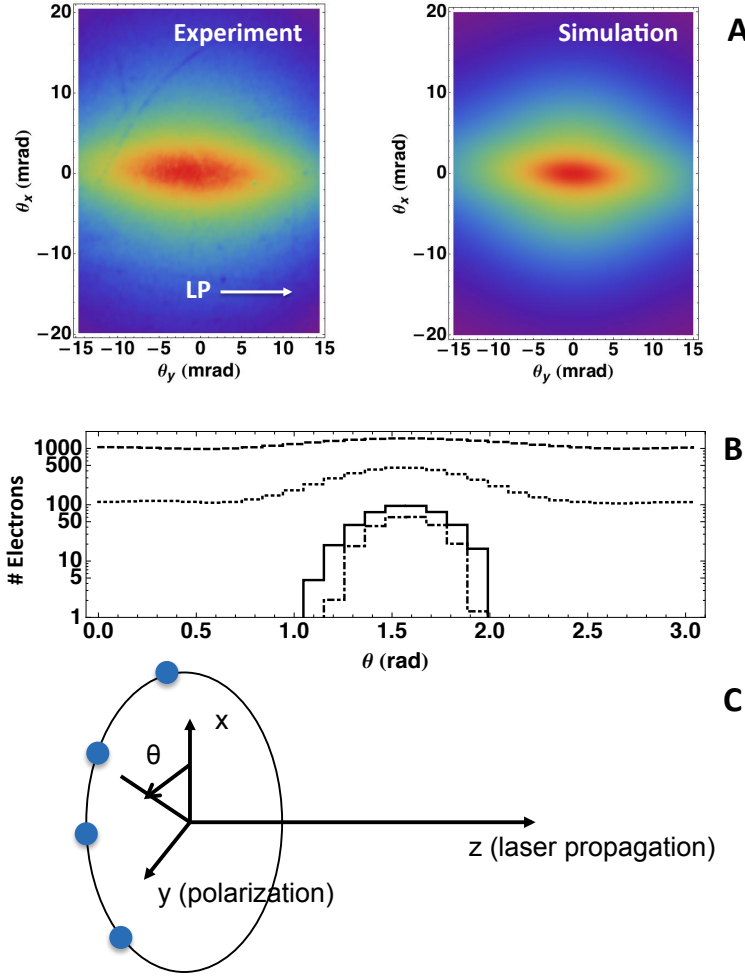
Figure 7. (A) Measured and simulated betatron x-ray beam profiles, recorded on IP_a, scanned with a 200 μm pixel size. LP indicates the laser polarization direction. The number of electrons around the propagation axis (positive z direction) is shown in (B) for four distinct groups of electrons accelerated up to $\gamma = 100$, 200, 440, and 520 (dashed, dotted, solid, and dot-dashed lines, respectively). $\theta = 0$ is along the x (vertical) axis and the laser is polarized along $\theta = \pi/2$ rad (y horizontal axis) . (C) Geometry for the electron trajectories.

detector and fit with the function $(\omega/\omega_c)^2 K_{2/3}^2(\omega/\omega_c)$ following the same method and peak energy definition as in Fig. 6. The error bars reflect the range of peak energies that fit the measured spectrum. The experimental data of Fig. 8 are then fitted with two different theoretical spectra obtained from: (i) the synchrotron radiation asymptotic limit (Eq. 3) where $\hbar\omega_c = 20$ keV is fixed and θ is the observation angle, and (ii) the spectrum emitted by the multiple trajectories of Fig. 7, calculated from Eq. 2 where the vector $\vec{n}$ is adjusted with the observation angle. As seen in Fig. 8, the simple model does not reproduce the experimental angular dependence of the x-ray spectrum because it assumes that electrons oscillate along only one direction. Although the most energetic particles primarily oscillate along the laser polarization axis, a larger number
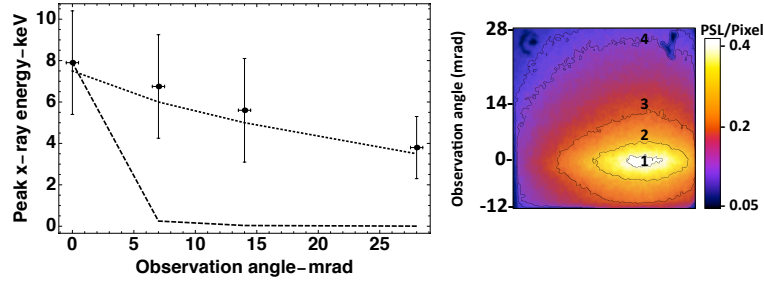
Figure 8. (Left) Peak experimental betatron x-ray energy as a function of the angle of observation (dots with error bars). The spectrum was measured on axis and at 7 mrad, 14 mrad and 28 mrad corresponding to respective vertical positions 1, 2, 3, 4 indicated on right side of the figure, which shows the beam profile on the first spectrometer channel. The two curves show the theoretical peak energy for Eq. 3 (dashed line) and the full set of electron trajectories (dotted line).

of lower-energy electrons oscillate with a wider range of angles in the transverse plane. This results in a softer decrease of the peak x-ray energy with increasing observation angles.

5.2. Comparison of several shots

We now compare the spectral and spatial properties of betatron x-ray beams obtained under different conditions, starting with the on-axis betatron x-ray spectrum. During this experimental campaign, we did several shots where it is also possible to do a similar analysis as the one presented above. However, shots need to be treated on a case-by-case basis and analyzed manually, because each was done under different experimental conditions (laser energy, electron density, gas composition). The following section reiterates the steps of our analysis by comparing the detailed characteristics (on axis spectrum, electron oscillation amplitude, orientation of the trajectories, spectrum angular dependence) of two shots.

By using the image plate sensitivity numbers from Ref [27] and the spectral distribution inferred from our measurements, we estimate the x-ray yield to be on the order of $10^8 - 10^9$ photons/pulse. This uncertainty due to the combination of several factors: uncertainty on the calibration itself, on the image plate thickness, and large shot-to-shot fluctuations during our experiment.

5.2.1. On axis spectral data and critical energy Figure 9 shows the data obtained for three different shots, with fits corresponding to different critical energies for the spectrum observed on axis. Each shot was done with a 10-mm long gas cell, with the following parameters. Shot 1: laser energy $E = 5.3$ J, $a_0 = 2.33$, 100 % He at $n_e = 6 \times 10^{18}$ cm^{-3}. Shot 2: $E = 8.5$ J, $a_0 = 2.95$, 99 % He and 1 % N$_2$ at $n_e = 7 \times 10^{18}$ cm^{-3}. Shot 3: $E = 6.1$ J, $a_0 = 2.5$, 100 % He at $n_e = 5 \times 10^{18}$ cm^{-3}. The calculated a_0 values include a ∼50% coupling of laser energy into the wake, typical for our experiments. For

each shot, we measure the dose in channels 1-6 of the detector and fit with the function $(\omega/\omega_c)^2 K_{2/3}^2(\omega/\omega_c)$ following the method defined for the analysis of the Fig. 6 data (Shot 1). In Fig. 9 we show the results of fits calculated for critical energies $\hbar\omega_c$ of 10, 15, 20 and 30 keV. For Shot 3, which corresponds to a betatron spectrum with a $\sim$10 keV critical energy, the data recorded on the spectrometer is below the detection threshold for channel 3 and above.

5.2.2. Electron oscillation amplitude We now determine the electron oscillation amplitude for Shot 2, by using the on-axis betatron x-ray spectral data, and by calculating the electron trajectory with the Runge-Kutta algorithm and subsequent betatron radiation from Eq. 2, accumulated over the whole electron trajectory. A detailed analysis, similar to that shown in Fig. 6 (Shot 1), shows that we can fit the spectral data of Shot 2 with the spectrum produced by an electron where the initial injection radius is adjusted to $r_0 = 5$ μm to fit the upper part of the error bars in our data. The results of this analysis are shown in Fig. 10, with the corresponding measured electron energy spectrum. The simulation parameters (time and frequency steps) are identical for Shot 1 and for Shot 2. For Shot 2, the initial conditions are also determined by the experimental measurements. In this case, the electron density is $n_e = 7 \times 10^{18}$ cm^{-3}, $\alpha = 0.86$, the electron final energy is 223 MeV ($\gamma \simeq 436$), and the electron initial energy is determined by $\gamma_\Phi = \omega_0/\sqrt{3}\omega_p = 9.1$.

5.2.3. Beam profile and orientation of trajectories The experimental and simulated beam profiles for Shot 2 are shown in Fig. 11. The principle is similar to the calculation presented in Fig 7: using a least-squares fitting method, the orientation of the electron trajectories for three groups of electrons is adjusted until the simulated beam profile matches the experimental one. For the simulation, the particles are also distributed on a circle of radius $r_0 = 5$ μm in the transverse (x, y) plane with angular steps of $\pi/30$. As for Shot 1, $\theta = 0$ is along the x axis and the laser is polarized along y ($\theta = \pi/2$). In Fig 11 (b), we show this number of electrons as a function of θ, for three groups of electrons with different final energies representative of the overall measured spectrum displayed in Fig. 10 (with extrapolation for the lower electron energies). As for Shot 1, a similar trend is observed, where electrons accelerated to higher energies oscillate primarily along the laser polarization direction.

5.2.4. Angular dependence of the betatron x-ray spectrum Finally, we compare the measured angular dependence of the x-ray spectrum for Shot 1 and Shot 2, as shown in Fig. 12. We measure a similar decrease of the peak energy from ~ 10 keV on axis to lower values at higher observation angles.
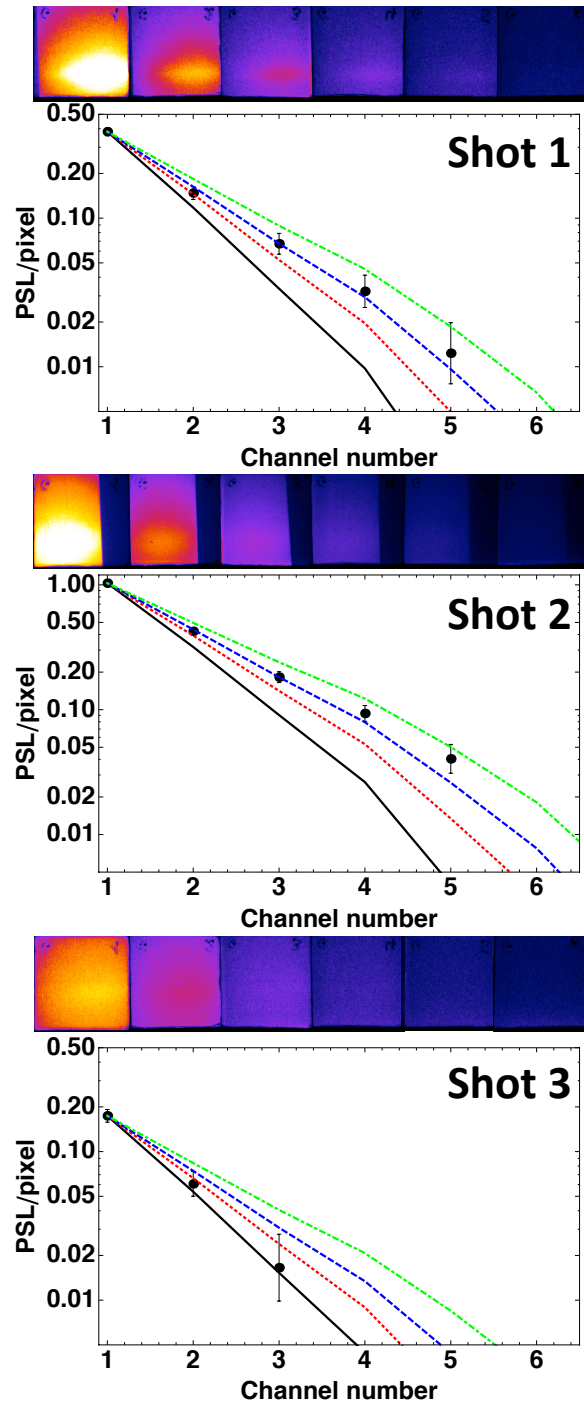
Figure 9. X-ray images, recorded on the stacked image plates spectrometer for channel 1-6, for three different shots (see text for parameters). The corresponding graphs are the x-ray spectrometer dose (dots with error bars), in photostimulated luminescence, PSL, per pixel. For each case, we show the calculated dose (normalized to the first data point), for betatron spectra with critical energies of 10 keV, 15 keV, 20 keV and 30 keV (solid, dotted, dashed and dot-dashed lines, respectively).
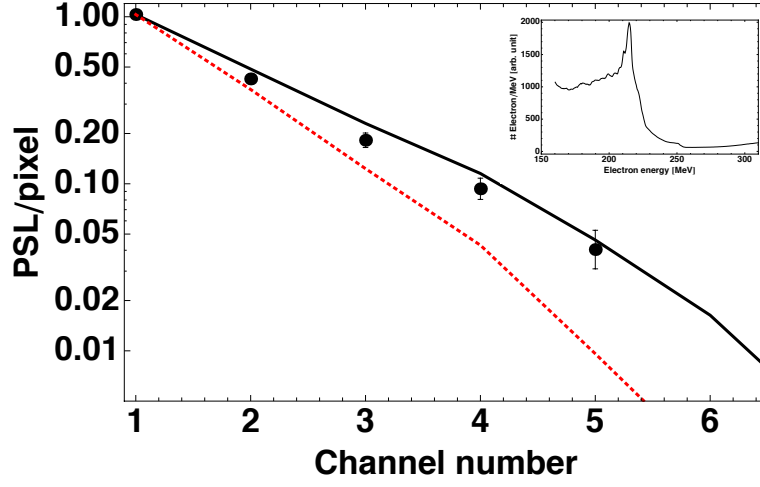
Figure 10. X-ray spectrometer dose (dots with error bars) for Shot 2, in photostimulated luminescence, PSL, per pixel. Calculated dose (normalized to the first data point), for the radiation produced by an electron injected 5 μm and 4 μm off-axis, and accelerated up to 223 MeV (solid and dotted line, respectively). The corresponding measured electron energy spectrum is shown in the inset.
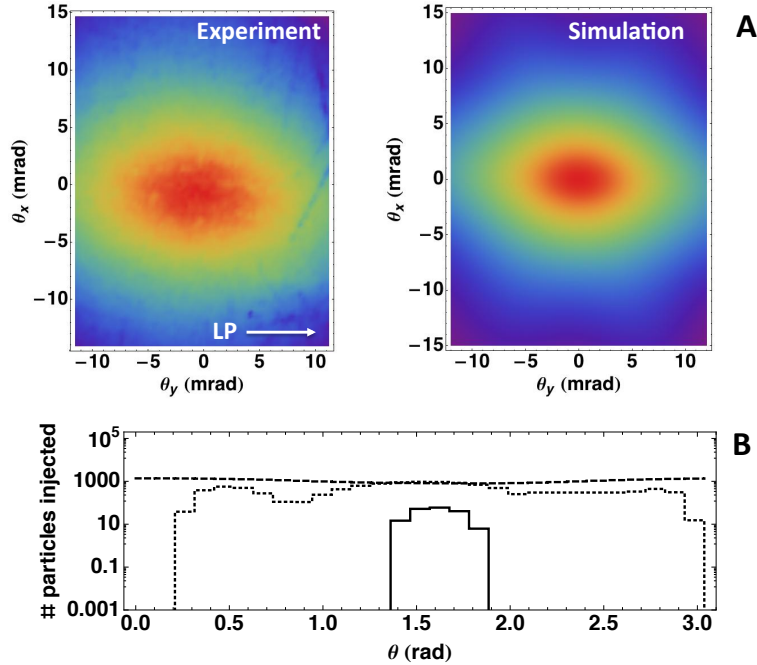

Figure 11. (A) Measured and simulated betatron x-ray beam profiles for Shot 2, recorded on IP$_a$, scanned with a 200 μm pixel size. The number of electrons around the propagation axis (positive z direction) is shown in (B) for three distinct groups of electrons accelerated up to $\gamma = 100$, 200, and 438 (dashed, dotted and solid lines, respectively). $\theta = 0$ is along the x (vertical) axis and the laser is polarized along $\theta = \pi/2$ rad (y horizontal axis).
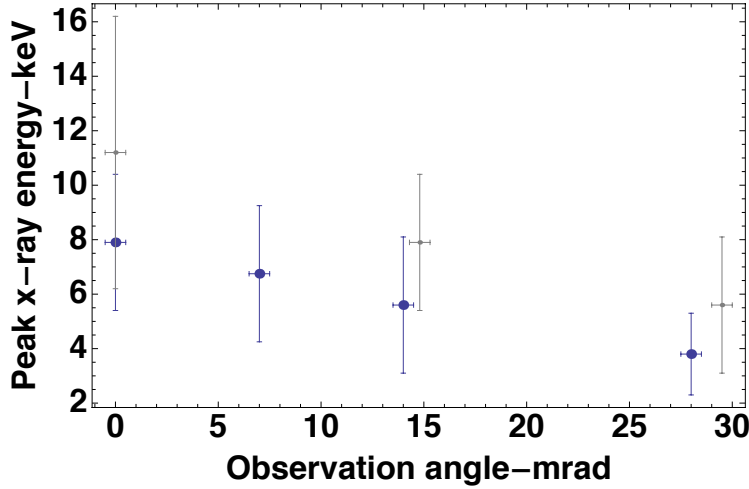
Figure 12. Comparison of the measured x-ray spectrum peak energy for Shot 1 (large dots with error bars) and Shot 2 (small dots with error bars), as a function of the observation angle.

5.3. Discussion

In our experiments, we have observed that for a given shot, electrons with different energies oscillate about the same axis but in different planes. In addition, we have observed shot-to-shot fluctuations of the x-ray beam profile for different laser and plasma parameters, but the beam profiles (and trajectories) tend to be all oriented along the same direction. We have several hypotheses to explain the anisotropy observed in the electron distribution in Fig. 3 (b). In our case, the high-energy particles oscillate primarily along the laser polarization direction. This is suggestive of these particles gaining energy from the wakefield and interacting with the transverse laser field [29]. The lower energy particles have a more isotropic distribution around the propagation axis possibly because they are injected into the wake at a later time, when the laser pulse has already undergone substantial longitudinal pulse compression [30]. At $n_e = 6 \times 10^{18}$ cm^{-3} and for a laser power P = 44 TW (50% coupling efficiency), the dephasing length $L_{dp}[\mathrm{cm}] \simeq (P[\mathrm{TW}])^{1/6}(10^{18}[\mathrm{cm}^{-3}]/n_e)^{4/3} \simeq 0.2^{+0.13}_{-0.04}$ cm is shorter than the length of the gas cell, and the most energetic electrons may interact with the back of the laser pulse to oscillate primarily in the direction of laser polarization. Betatron x-rays with spectra peaking at 150 keV and containing $\sim 10^8$ photons have been reported [31], due to the interaction of the electron bunch with the laser [32]. The other effect that can strongly influence the direction of the electron oscillations and subsequent betatron radiation is pulse front tilt [33]. In this case, controlling the pulse front tilt by voluntarily misaligning one of the gratings of the laser compressor system and producing an asymmetric laser intensity profile can lead to an asymmetric wake. Experiments and simulations have shown that by doing this, the direction of the oscillations and the x-ray polarization are anisotropic [34]. Detailed measurements and simulations, where the betatron beam

profile can be monitored while changing the laser polarization or pulse front tilt, should better explain the origin of the observed anisotropy in our experiments.

6. Conclusion

In conclusion, we have implemented a new betatron x-ray source diagnostic capability in laser-wakefield acceleration experiments. It can measure both the single-shot beam profile and x-ray spectrum at different angles of observation. This enables a three dimensional reconstruction (as opposed to electron beam size only) of the electron trajectories to understand the detailed physics of the injection and acceleration mechanisms without the need of extensive Particle In Cell simulations. We also have observed that the betatron x-ray energy decreases as the observer looks further away from the axis of propagation, and that these observations can be explained by assuming an anisotropic distribution of the electron energy spectrum. Obtaining the full spectral and spatial properties of the betatron radiation in a singe shot to understand the physics of the electron dynamics in the plasma is essential for future implementation of the betatron x-ray source on large-scale, low repetition rate laser systems. We expect that betatron radiation will become a powerful x-ray probe for x-ray imaging [35] and absorption spectroscopy [36] techniques in high energy density science experiments.

[1] Tajima T and Dawson J M 1979 *Phys. Rev. Lett.* **43** 267–270

[2] Mangles S P D, Murphy C D, Najmudin Z, Thomas A G R, Collier J L, Dangor A E, Divall E J, Foster P S, Gallacher J G, Hooker C J, Jaroszynski D A, Langley A J, Mori W B, Norreys P A, Tsung F S, Viskup R, Walton B R and Krushelnick K 2004 *Nature* **431** 535–538

[3] Faure J, Glinec Y, Pukhov A, Kiselev S, Gordienko S, Lefebvre E, Rousseau J P, Burgy F and Malka V 2004 *Nature* **431** 541–544

[4] Geddes C G R, Toth C, Tilborg J V, Esarey E, Schroeder C B, Bruhwiler D, Nieter C, Cary J and Leemans W P 2004 *Nature* **431** 538–541

[5] Esarey E, Shadwick B A, Catravas P and Leemans W P 2002 *Phys. Rev. E* **65** 056505

[6] Wang S, Clayton C E, Blue B E, Dodd E S, Marsh K A, Mori W B, Joshi C, Lee S, Muggli P, Katsouleas T, Decker F J, Hogan M J, Iverson R H, Raimondi P, Walz D, Siemann R and Assmann R 2002 *Phys. Rev. Lett.* **88** 135004

[7] Rousse A, Phuoc K T, Shah R, Pukhov A, Lefebvre E, Malka V, Kiselev S, Burgy F, Rousseau J P, Umstadter D and Hulin D 2004 *Phys. Rev. Lett.* **93** 135005

[8] Corde S, Phuoc K T, Lambert G, Fitour R, Malka V and Rousse A 2013 *Rev. Mod. Phys.* **85** 1–47

[9] Kneip S, McGuffey C, Martins J L, Martins S F, Bellei C, Chvykov V, Dollar F, Fonseca R, Huntington C, Kalintchenko G, Maksimchuk A, Mangles S P D, Matsuoka T, Nagel S R, Palmer

C A J, Schreiber J, Phuoc K T, Thomas A G R, Yanovsky V, Silva L O, Krushelnick K and Najmudin Z 2010 *Nat. Phys.* **6** 980–983

[10] Shah R C, Albert F, Phuoc K T, Shevchenko O, Boschetto D, Pukhov A, Kiselev S, Burgy F, Rousseau J P and Rousse A 2006 *Phys. Rev. E* **74** 045401(R)

[11] Phuoc K T, Corde S, Shah R, Albert F, Fitour R, Rousseau J P, Burgy F, Mercier B and Rousse A 2006 *Phys. Rev. Lett.* **97** 225002

[12] Phuoc K T, Fitour R, Tafzi A, Garl T, Artemiev N, Shah R, Albert F, Boschetto D, Rousse A, Kim D E, Pukhov A, Seredov V and Kostyukov I 2007 *Phys. Plasmas* **14** 080701

[13] Albert F, Shah R, Phuoc K T, Fitour R, Burgy F, Rousseau J P, Tafzi A, Douillet D, Lefrou T, and Rousse A 2008 *Phys. Rev. E* **77** 056402

[14] Fourmaux S, Corde S, Phuoc K T, Leguay P M, Payeur S, Lassonde P, Gnedyuk S, Lebrun G, Fourment C, Malka V, Sebban S, Rousse A and Kieffer J C 2011 *New J. Phys.* **13** 033017

[15] Corde S, Thaury C, Lifschitz A, Lambert G, Phuoc K T, Davoine X, Lehe R, Douillet D, Rousse A and Malka V 2013 *Nat. Comm.* **4** 1501

[16] Plateau G R, Geddes C G R, Thorn D B, Chen M, Benedetti C, Esarey E, Gonsalves A J, Matlis N H, Nakamura K, Schroeder C B, Shiraishi S, Sokollik T, Tilborg J V, Toth C, Trotsenko S, Kim T S, Battaglia M, Stohlker T and Leemans W P 2012 *Phys. Rev. Lett.* **109** 064802

[17] Schnell M, Savert A, Landgraf B, Reuter M, Nicolai M, Jackel O, Peth C, Thiele T, Jansen O, Pukhov A, Willi O, Kaluza M C and Spielmann C 2012 *Phys. Rev. Lett.* **108** 075001

[18] Kneip S, McGuffey C, Martins J L, Bloom M S, Chvykov V, Dollar F, Fonseca R, Jolly S, Kalintchenko G, Krushelnick K, Maksimchuk A, Mangles S P D, Najmudin Z, Palmer C A J, Phuoc K T, Schumaker W, Silva L O, Vieira J, Yanovsky V and Thomas A G R 2012 *Phys. Rev. ST Accel. Beams* **15** 021302

[19] Martins J, Martins S, Fonseca R and Silva L 2009 Radiation post-processing in pic codes *Harnessing Relativistic Plasma waves as Novel Radiation Sources from Terahertz to X-rays and Beyond* (*Proc. SPIE* vol 7359) ed Dino A Jaroszynski A R pp 73590V–1–73590V–8

[20] Lu W, Tzoufras M, Joshi C, Tsung F S, Mori W B, Vieira J, Fonseca R A and Silva L O 2007 *Phys. Rev. ST Acc. Beams* **10** 061301

[21] Jackson J 1998 *Classical Electrodynamics*

[22] Blumenfeld I, Clayton C E, Decker F J, Hogan M J, Huang C, Ischebeck R, Iverson R, Joshi C, Katsouleas T, Kirby N, Lu W, Marsh K A, Mori W B, Muggli P, Oz E, Siemann R H, Walz D and Zhou M 2006 *Nature* **445** 741–744

[23] Clayton C E, Ralph J E, Albert F, Fonseca R A, Glenzer S H, Joshi C, Lu W, Marsh K A, Martins S F, Mori W B, Pak A, Tsung F S, Pollock B B, Ross J S, Silva L O and Froula D H 2010 *Phys. Rev. Lett.* **105** 105003

[24] Pollock B B, Clayton C E, Ralph J E, Albert F, Davidson A, Divol L, Filip C, Glenzer S H, Herpoldt K, Lu W, Marsh K A, Meinecke J, Mori W B, Pak A, Rensink T C, Ross J S, Shaw J, Tynan G R, Joshi C and Froula D H 2011 *Phys. Rev. Lett.* **107** 045001

[25] Pollock B B, Ross J, Tynan G R, Divol L, Glenzer S H, Leurent V, Palastro J P, Ralph J, Froula D, Clayton C E, Marsh K, Pak A E, Wang T and Joshi C 2009 Two-screen method for determining electron beam energy and deflection from laser wakefield acceleration Proceedings of PAC09, Vancouver, BC Canada pp 3035–3037

[26] Chen C D, King J A, Key M H, Akli K U, Beg F N, Chen H, Freeman R R, Link A, Mackinnon A J, MacPhee A G, Patel P K, Porkolab M, Stephens R B and Woerkom L D V 2008 *Rev. Sc. Instr.* **79** 10E305

[27] Maddox B R, Park H S, Remington B A, Izumi N, Chen S, Chen C, Kimminau G, Ali Z, Haugh M J and Ma Q 2011 *Rev. Sc. Instr.* **82** 023111

[28] Albert F, Pollock B, Shaw J, Marsh K A, Ralph J E, Chen Y H, Alessi D, Pak A, Clayton C E, Glenzer S H and Joshi C 2013 *Phys. Rev. Lett. (in press)*

[29] Mangles S P D, Thomas A G R, Kaluza M C, Lundh O, Lindau F, Persson A, Tsung F S, Najmudin Z, Mori W B, Wahlstrom C G and Krushelnick K 2006 *Phys. Rev. Lett.* **96** 215001

[30] Faure J, Glinec Y, Santos J J, Ewald F, Rousseau J P, Kiselev S, Pukhov A, Hosokai T and Malka V 2005 *Phys. Rev. Lett.* **95** 205003

[31] Cipiccia S, Islam M R, Ersfeld B, Shanks R P, Brunetti E, Vieux G, Yang X, Issac R C, MWiggins S, HWelsh G, Anania M P, Maneuski D, Montgomery R, Smith G, Hoek M, Hamilton D J, Lemos N R C, Symes D, Rajeev P P, Shea V O, Dias J M and Jaroszynski D A 2011 *Nat. Phys.* **7** 867

[32] Thomas A G R and Krushelnick K 2009 *Phys. Plasmas* **16** 103103 ISSN 1070-664X

[33] Popp A, Vieira J, Osterhoff J, Major Z, Hrlein R, Fuchs M, Weingartner R, Rowlands-Rees T P, Marti M, Fonseca R A, Martins S F, Silva L O, Hooker S M, Krausz F, Gruner F and Karsch S 2010 *Phys. Rev. Lett.* **105** 215001

[34] Schnell M, Savert A, Uschmann I, Reuter M, Nicolai M, Kampfer T, Landgraf B, Jackel O, Jansen O, Pukhov A, Kaluza M C and Spielmann C 2013 *Nat. Commun* **4** 2421

[35] Hicks D and et al 2012 *Phys. Plasmas* **19** 122702

[36] Benuzzi-Mounaix A, Dorchies F, Recoules V, Festa F, Peyrusse O, Levy A, Ravasio A, Hall T, Koenig M, Amadou N, Bambrink E and Mazevet S 2011 *Phys. Rev. Lett.* **107** 165006